Atomistic simulations of He bubbles in Beryllium

Jianqi Xi[*#1], *Yeqi Shi*[#1], *Vitaly Pronskikh*[2], *Frederique Pellemoine*[2], *Dane Morgan*[1], *Izabela Szlufarska*[*1]

1. University of Wisconsin-Madison, Department of Materials Science & Engineering, Madison, WI, USA

2. Fermi National Accelerator Laboratory, Batavia, Illinois 60510, USA

Abstract

Formation of He bubbles can have a significant effect on the microstructural evolution and properties of irradiated materials. Here, we use atomistic simulations based on machine learning potentials to investigate the fundamental behavior of He bubbles in Be, with a specific focus on the shape, stability, and diffusivity of bubbles. Stability of He bubbles is quantified in terms of formation energies, which are determined as a function of the ratio of He/V. We find that He bubbles become unstable with respect to plastic deformation through punch-out dislocations around the bubble when the He/V ratio is larger than ~1.25, and the punch-out process induces the change of the regular bubble shape. In general, the bubble shape of He in Be is found to be ellipsoid-like. It is also found that for a fixed He/V ratio, the bubble attracts vacancies to become larger in size. If the bubble size is constant, the bubble attracts additional He atoms until the punch-out reaction occurs. The dominant diffusion mechanism of He bubbles changes from surface diffusion to volume diffusion as the temperature is increased, with a crossover occurring at about 900 K.

Keywords

He bubble, Beryllium, Stability, Diffusivity

1. Introduction

Beryllium (Be) has attracted a lot of attention in the context of applications that involve radiation [1–8] because of the excellent radiation response properties of this material, such as the low atomic number, low neutron-capture cross-section, and high neutron scattering cross-section. For example, Be is used as a neutron moderator in nuclear fission reactors [1–3] and it is being considered for the first wall of the ITER nuclear fusion reactor [3–5]. Be has been also used as the target material and beam window in high-energy particle accelerators [6–8]. In those applications, Be is exposed to high-radiation environments, which leads to the accumulation of nuclear reaction products, especially helium. In these applications the helium production rate is relatively high, *e.g.*, ~1000 appm/dpa (atomic parts per million/displacement per atom) for typical Be targets. As a result, He atoms tend to aggregate in the form of large extended defects, such as bubbles or platelets, which in turn can significantly degrade the structural integrity of the

[*] *Department of Materials Science and Engineering, University of Wisconsin, Madison, WI, 53706, USA. E-mail: szlufarska@wisc.edu, jxi4@wisc.edu; Tel: +1-608-265-5878*

[#] *Co-first author*

material. For instance, earlier studies have shown that the formation of He bubbles in Be can cause significant swelling, enable crack propagation, and eventually cause failure by fracture [6,7]. Experimentally, many studies on He bubble formation in Be have been reported in the context of nuclear reactor applications. Generally, formation of He bubbles is strongly dependent on the irradiation temperature. For example, Chakin *et al.* reported a lack of He bubbles in Be irradiated at room temperature for 15 years up to a fast neutron fluence of 5.7×10^{22} n/cm^2 and the corresponding He production of 11,500 appm [9]. In a different study, Klimenkov *et al.* investigated He bubble evolution in Be under thermal and fast neutron irradiation at temperatures ranging from 387 ℃ to 695 ℃, in which the He production was in the range from 2,090 to 5,524 appm [2,3]. In those studies, He bubbles were observed at all temperatures considered, which suggests that defects (either He interstitials or Be vacancies or both) are mobile within that temperature regime. The authors also found that with an increasing irradiation temperature, the average diameter of He bubbles increased from 7.5 to 90 nm, and the bubbles were found in the form of ellipsoidal-like shapes with the long ellipse axis in the {0001} basal plane. While the aforementioned experimental studies of neutron irradiated Be provide very useful guidance on the He bubble evolutions in the nuclear applications, they provide limited understanding and it is therefore not known at present to what extent these results can be translated to understand radiation effects in Be exposed to new temperature, flux, and fluence conditions. This lack of knowledge of transferability is a significant issue for design of targets in future particle accelerators, in which materials will be exposed to radiation with new conditions of very high power and high energy pulsed proton beams. Therefore, a fundamental understanding of He behavior in Be is essential for predicting materials behavior under conditions that have not been investigated experimentally.

In general, mechanisms leading to bubble formation and evolution in irradiated materials have been extensively investigated, in particular in metals with cubic structures [10–15]. However, most available studies for Be concern the first stages of bubble formation, and in particular the stability and migration properties of a single He atom, as well as interactions between He atoms and vacancies [16–18]. Little is known about the properties of fully grown He bubbles in Be. Specifically, important factors to consider are the shape and stability of bubbles and the diffusivity of bubbles. These properties significantly impact the microstructural evolutions in irradiated materials and provide essential input for multiscale models of microstructural evolutions. For example, previous atomistic simulations in tungsten have shown that bubbles with a high ratio of He to vacancies (He/V ratio) tend to punch out dislocation loops to release the internal pressure of the bubble, which causes local structural changes [12,19–21]. However, considering the different plastic properties of tungsten and beryllium, the release of bubbles' internal pressure in beryllium could be much different, and it is therefore necessary to examine whether similar or different plasticity mechanisms occur in beryllium.

Here, we report results of atomistic simulations of helium bubbles in beryllium with a focus on the shape of bubbles in Be as a function of size, as well as their stability and diffusivity as a

function of the ratio of He/V. Those properties of bubbles are necessary to predict He bubble evolution using multiscale models.

2. Simulation methods

Large-scale Atomic/Molecular Massively Parallel Simulator (LAMMPS) software [22] is used to perform molecular dynamics (MD) simulations. The interatomic forces for Be-Be were described using the spectral neighbor analysis potential (SNAP), which is a machine learning-based potential developed by Thompson *et al.* [23]. The basic idea of SNAP machine learning potential is to use bispectrum component $\mathbf{B}^{\boldsymbol{i}}$ derived from the density of neighbor atoms around a central atom *i* in order to train a linear regression model. Energy and force on atom *i* are described using the following equations

$$E^i_{\mathrm{SNAP}} = \beta_0 + \sum_{k=1}^{K} \beta_k B^i_k = \beta_0 + \boldsymbol{\beta} \cdot \mathbf{B}^{\boldsymbol{i}} \quad \#(1)$$

$$\mathbf{F}^{\boldsymbol{j}}_{\mathbf{SNAP}} = -\boldsymbol{\nabla}_{\boldsymbol{j}} \sum_{\boldsymbol{i=1}}^{\boldsymbol{N}} E^i_{\mathrm{SNAP}} = -\boldsymbol{\beta} \cdot \sum_{\boldsymbol{i=1}}^{\boldsymbol{N}} \frac{\partial \mathbf{B}^{\boldsymbol{i}}}{\partial \mathbf{r}^{\boldsymbol{j}}} \quad \#(2)$$

In Eq. (1), E^i_{SNAP} is the potential energy of atom *i* predicted by SNAP model, B^i_k is the *k*th bispectrum component (K components in total) of atom *i* derived from the density of its neighbor atoms, β_k is its associated linear coefficient, β_0 is the constant energy contribution of atom *i*. The K-order vectors represent linear coefficient and bispectrum can be written as $\boldsymbol{\beta}$ and $\mathbf{B}^{\boldsymbol{i}}$, respectively. In Eq. (2), $\mathbf{F}^{\boldsymbol{j}}_{\mathbf{SNAP}}$ is the force on atom *j*, N is the number of its neighbor atoms, $\mathbf{r}^{\boldsymbol{j}}$ is its position vector. The parameters for the SNAP model used in this research are from Ref. [24]. This potential has been fit to Be data that includes defect formation energies and defect migration energy barriers in Be.

Interactions between He atoms (He-He) are described using an empirical potential developed by Juslin *et al.* [25]. The potential in Ref. [25] is based on the Beck potential [26] with the short-range interactions modified by Morishita *et al.* [27]. Interactions between He and Be atoms are calculated using the potential developed by Cusentino *et al* [28]. In this approach, the short-range interaction between He and Be atoms is described using the Ziegler-Biersack-Littmark (ZBL) potential [29], the medium-range interaction is described using a six-order polynomial, and the long-range interaction is described using a decaying exponential. The aforementioned potentials have been successfully used to describe the He implantation and evolution in WBe_2 intermetallic and W-Be amorphous systems [24].

We use the following equations to calculate the formation energy of point defect (PD) and He bubble in Be:

$$E_f(\mathrm{PD}) = E_{def} - N_{Be}\mu_{Be} - N_{He}\mu_{He}\,. \quad (3a)$$

$$E_f(\mathrm{He}_m\mathrm{V}_n) = (E_{def} - (N - n_V)\mu_{Be} - m_{He}\mu_{He})/n_V\,. \quad (3b)$$

Here, E_f is the defect formation energy, E_{def} is the potential energy of a defective Be sample, and N_{Be} and N_{He} in Eq. (3a) are the number of Be and He atoms in the defective Be sample,

respectively. N, n_V, and m_{He} in Eq. (3b) are the total number of Be in the perfect sample, the number of vacancies and He atoms in the defective sample, respectively. μ_{Be} and μ_{He} are the chemical potentials of Be and He, where take hexagonal phased Be metal and isolated He atom as a reservoir, respectively. μ_{Be} is calculated to be -3.274 eV from the potential with a molecular static (MS) calculation [30,31] with reference to the isolated Be atom. μ_{He} is 0 eV with a reference to the isolated He atom as the reference is the same as the reservoir. For the calculations of the formation energy of point defects and small He-V clusters, the simulation system (we call this system 1) is in the dimension of 1.6 nm × 1.4 nm × 1.5 nm, and the perfect simulation cell contains 384 atoms. The system size is increased when considering the large He bubbles, where we use what we call system 2. In system 2 the number of Be vacancies in the bubbles varies from 876 to 4040, the total number of atoms in each perfect simulation cell is 64,000, and the system has dimensions 9.0 nm × 7.8 nm × 7.1 nm. Note that in all cases when we refer to a number of vacancies in a bubble it is actually the number of Be removed from region at the initialization of the calculation. As the system may relax in ways strongly dependent on the number of vacancies and He the value of the number of vacancies may have a complex relationship to the final relaxed size of the bubble. For each bubble size, we perform separate simulations for different He/vacancy (He/V) ratios, and we vary this ratio from 0.1 to 2. The canonical ensemble (NVT) is used for the simulations. In all the above simulations we equilibrated the system at 700 K for 200 ps, and then quenched to 0 K over 200 ps. We used a timestep of 1 fs. Additional energy minimization is performed after the system has been quenched to 0 K using conjugate gradient (CG) optimization. In system 2, we generate the bubble structure from the Wulff construction based on the calculated surface energy (see Table. 2) in the usage of WulffPack [32]. The initial volume of each bubble is determined by the number of vacancies in the bubble.

To validate the accuracy of our MD simulations, additional density functional theory (DFT) calculations are performed. All the DFT calculations are performed with the Vienna Ab-Initio Simulation Package using the projector augmented wave (PAW) method [33]. The exchange-correlation is treated in the generalized gradient approximation (GGA) as parameterized by Perdew, Burke, and Ernzerhof (PBE) [33]. One 4×3×3 supercell is used that contains 144 atoms. All computations are performed with a cutoff energy of 500 eV for the plane-wave basis set and with spin-polarized conditions. The k-point mesh is set to 3×3×3. Errors in defect formation energies from the cutoff energy and k-point convergence are less than 1 meV/atom. All lattice parameters and atomic coordinates are fully relaxed until the forces on each atom are smaller than 1×10^{-3} eV/Å. The chemical potential of Be and He in the DFT calculations are -3.767 eV and 0 eV, respectively, using the same reference and resource in the above MS calculations.

3. Results and Discussion

3.1 Comparison of defect formation energies from MD and DFT

Table 1 Comparison of the calculated lattice constants and the point defect formation energy between MD and DFT.

Parameter	MD	DFT
Lattice constant a (Å)	2.257	2.266
Lattice constant c (Å)	3.547	3.561
Be vacancy (eV)	0.642	0.608
Be interstitial (eV)	4.013	4.306
He interstitial (eV)	5.225	5.833
He substitution (eV)	2.709	3.322

As described in Ref. [24], the interatomic potentials used in this work have been successfully employed to describe the He bubble evolutions in WBe_2 intermetallic and W-Be amorphous systems. Here we test the accuracy of the potentials for the He bubbles in pure Be. Formation energies of point defects are summarized in Table 1, which shows a relatively good agreement between MD simulations and DFT calculations. We can see that the formation energy of He interstitial is much higher than that of He substitutional defect, which suggests that the He defect is energetically unfavorable to exist as an interstitial in Be, and radiation-induced He defects will prefer to occupy the Be vacancy to form the He substitution. We further calculate the formation and binding energies of He atom in various small He-V clusters for different He/V ratios. The results are shown in Fig. 1. The trends from MD (dashed lines) and DFT (solid lines) are in a relatively good agreement with each other. These results validate the use of these fitted potentials for our calculations.

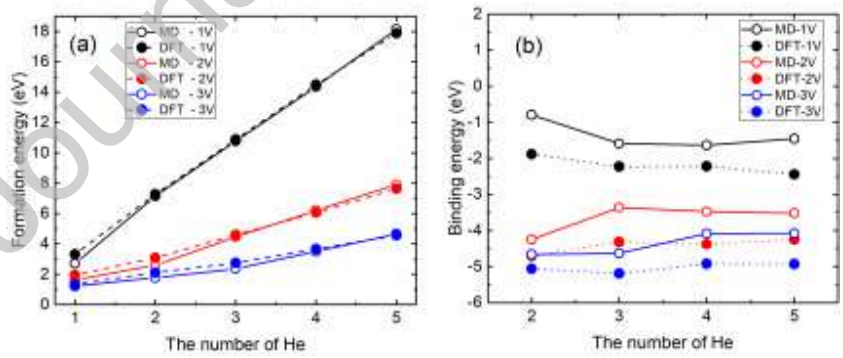

Fig. 1. (a) Formation energies of small He-V clusters with the different numbers of He and V. (b) Binding energies of He atom in the small He-V clusters with the different numbers of He and V. Black, red, and blue lines represent the clusters containing 1, 2, and 3 vacancies, respectively. Solid and dashed lines represent the formation energy calculated using DFT and MD, respectively.

3.2 The shape and stability of He bubbles in Be

Table 2 Comparison of the calculated surface energy between MD and DFT.

Surface	MD ($eV/Å^2$)	DFT ($eV/Å^2$)
$\{0001\}$	0.0714	0.1058
$\{10\bar{1}0\}$	0.1056	0.1183
$\{10\bar{1}1\}$	0.1045	0.1185
$\{20\bar{2}1\}$	0.1034	0.1173
$\{21\bar{3}0\}$	0.1363	0.1293

It has been reported that the shape of He bubbles in metals could be spherical-like, faceted, or ellipsoidal-like [10,34]. The specific shape of the bubble can impact its stability. For example, the ellipsoidal-like bubble in tungsten tends to punch out dislocation loops above the bubble in order to become a more spherical-like one [21]. Before we quantify the stability of He bubble in Be, we first determine the shape of the most stable bubbles. Generally, a He bubble can be regarded as a void that contains a large number of He atoms. The build-up of He gas can cause high internal pressure inside the bubble. In our approach, we first determine the shape of the void formed by vacancies. Toward this end, we use the Wulff construction, which is based on the concept that the crystal seeks to minimize its total surface energy subject to the constraint of fixed volume [35]. Crystal planes with lower surface energies and small miller indices tend to contribute more to the equilibrium shape of the void. In the case of Be, the surfaces $\{0001\}$, $\{10\bar{1}0\}$, $\{10\bar{1}1\}$, $\{20\bar{2}1\}$, and $\{21\bar{3}0\}$ are expected to dominate the shape construction. The energies of those surfaces are calculated from the MD simulations and are similar to those obtained from DFT calculations (see Table 2). The $\{0001\}$ basal plane is found to have the lowest surface energy, suggesting the basal plane would constitute a high fraction of the surface area of the void. Using surface energies from the present MD calculations listed in Table 2, we determine the equilibrium Wulff shape of void in Be. As shown in Fig. 2, the void in Be has an ellipsoid-like shape. According to the Wulff construction, the ratio of semi-axes of the ellipsoid is determined by the ratio of surface energies between $\{0001\}$ and $\{10\bar{1}0\}$, which is around 0.676.

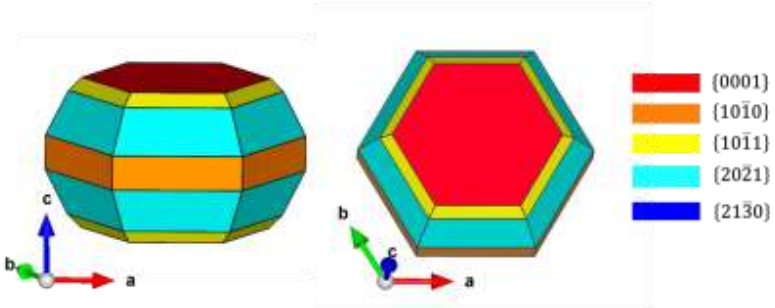

Fig. 2. Equilibrium Wulff shape created using surface energies from the result of MD simulation in Table 2 illustrated in the VESTA software. The ratio of semi-axes of the ellipsoid is around 0.676.

To investigate the shape and stability of He bubbles in Be, we add certain numbers of He atoms into one void, consisting of 3452 vacancies, and then relax the system at 700 K for 200 ps. The total energy and pressure of the system are plotted as a function of the He/V ratio in the bubble in Fig. 3. For He/V ratios smaller than ~0.4, both the pressure (Fig. 3(a)) and the total energy of the system (Fig. 3(b)) are relatively constant and independent of the He/V ratio. This is a regime where He atoms in the void can be regarded as inert gas atoms, *i.e.*, the He-He interactions are negligible. When the He/V ratio is larger than 0.4, both the pressure and the total energy of the system begin to increase as well. However, we did not observe any displacement of Be atoms from their lattice positions, instead only a small shift around their lattice sites was observed. This behavior is similar for He/V ratios up to ~1.25. At and above this ratio, the internal pressure of He bubble is high enough to punch out dislocations around the bubble. In this regime, we found that Be atoms surrounding the bubble are displaced from their lattice sites and form interstitials. In addition to the case of bubble with 3452 Be vacancies shown in Fig. 3, we also test bubbles with different sizes containing 876, 1406, 2040, 2452, 2928, and 4040 Be vacancies. We found qualitatively similar results in that the punch-out reactions occur as the He/V ratio is larger than ~1.25 (See Fig. S1). Our observations are different from the previously reported punch-out reaction in tungsten, where the reaction occurs for the ratio of He/V equal or larger than ~ 4-5 [20]. This result is understandable when considering the different yield strengths of beryllium and tungsten (~240 MPa for Be and ~750 MPa for W at room temperature) and also the small critical shear stresses for the basal slip in beryllium [36]. Compared with tungsten, the softer beryllium metal suggests that the formation of dislocation in beryllium is easier than that in tungsten. Here it should be noted that this is the initial ratio before any reactions; and after punch-out reactions, the He/V ratio could be changed.

To determine whether the presence of He atoms changes the shape of the bubble, we perform MD simulations for systems with the He/V ratio of 0.2, 1.0, and 1.5 for additional 2 ns at 700 K. We found that when the ratio is smaller than 1.25, the shape of He bubbles remains as regular ellipsoid (see inserts in Fig. 3(a)). However, when the ratio is larger than 1.25, the punch-out reactions cause the He bubble to change shape and become irregular ellipsoids (see inset in Fig. 3(a)), which can affect the ratio of the semi-axes of the ellipsoid. Therefore, we assume the energies based on the Wulff construction are accurate for He/V ratios up to ~1.25 but above that the impact of the results is metastable energy. Even though those energies as the ratio above ~1.25 are stable within the MD simulation time scale, they might evolve significantly over a longer time. It is noted that for both the fission reactor conditions and the particle accelerator conditions, the ratio of He/V is smaller than 1.25 (See Table S1), therefore, the results shown here can be used for both conditions.

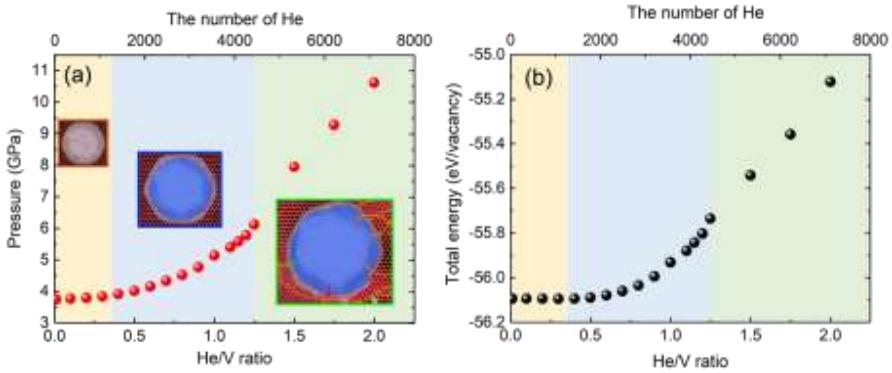

Fig. 3. (a) The pressure and (b) total energy of systems that include a He bubble made up of 3452 Be vacancies. The insert in (a) shows atomic structures of He bubbles with ratio of 0.2, 1.0, and 1.5 after relaxation for 200 ps at 700 K, respectively. In the inserts, red points are the Be atoms and the blue ones are He atoms. The punch-out dislocations are shown as lines and are determined using OVITO.

3.3 Formation of He bubbles in Be

Formation energies of bubbles are calculated using Eq. (3). To investigate relationships between bubble formation energy, bubble size, and He/V ratio, we calculate the formation energy of bubbles with different numbers of Be vacancies and different He/V ratios, as shown in Fig. 4. Here, we only consider bubbles without punch-out reactions and we use Wulff shapes and relaxation methods as described in Sec. 2. As described in Sec. 3.2, the bubbles largely maintain the Wulff shape during relaxation. Fig. 4 (a) shows that for a given He/V ratio, the bubble formation energy is always positive, which means that the bubble is always more stable than the isolated vacancies. Furthermore, the bubble formation energy per vacancy decreases with an increasing number of vacancies in the bubble (i.e., increasing bubble size). That means that He bubble prefers to attract vacancies in order to grow, but this attraction becomes weaker as the bubble grows. This trend is expected due to surface energy effects (i.e., the Gibbs-Thompson effect) and due to the decreasing ability of the vacancies to reduce the He pressure. Furthermore, all the curves appear to be leveling off, suggesting that for large enough number of vacancies the energy per vacancy (and the energy to add a vacancy) becomes nearly constant, as would be expected in the limit where surface energies and He pressure effects are negligible. We also note that the slope of the curves is more negative for higher He/V ratios, consistent with a larger contribution from the He pressure reduction for larger He/V ratios. The ability of He (or any gas) to make adding vacancies to a bubble more attractive is the fundamental energetics underlying the ability of gasses to stabilize cavities in many metallic systems. Fig. 4(b) shows that for a given bubble size (e.g., the number of vacancies in the bubble equal to ~3452), the formation energy of the bubble increases as the He/V ratio increases. This trend is expected as the He exerts a pressure, destabilizing the bubble at fixed number of vacancies. From Fig. 4(b) we can also see that the curve with He/V ratio is highly nonlinear, starting almost flat when the He/V ratio is smaller than ~0.4, and then accelerating much faster than linear for the larger He/V ratios. The result can be understood because for He/V ratio smaller than 0.4 the fraction of He within

the bubble is small enough that the interaction He with itself is negligible and essentially unaffected by changing amounts of He. We can qualitatively estimate when He-He interactions will become significant by determining at what He/V ratio the distance between He and He will be smaller than its stable nearest neighbor distance in its stable fcc structure (2.969 Å). For the faced-centered cubic He, the volume of He with nearest-neighbor distance 2.969 Å will be larger than the bubble volume for He/V ratio larger than 0.4. Thus we expect the energy curve to be quite flat for He/V<0.4, and above that ratio, we expect the repulsive interaction of He-He will increase the pressure of the system and thereby increase the bubble energy (See Fig. S2).

Based on the above results we can see that, for the He/V ratio smaller than ~0.4, the binding energy of one He atom in the bubble consisting of *m* He atoms and *n* vacancies will be predominantly determined by the formation energy of He interstitial in Be, i.e., $E_b = E_f(\mathrm{He}_m\mathrm{V}_\mathrm{n}) - E_f(\mathrm{He}_{m-1}\mathrm{V}_\mathrm{n}) - E_f(\mathrm{He}) \approx -E_f(\mathrm{He})$. For the He/V ratio between ~0.4 and ~1.25, the formation energy of He bubble as a function of He/V ratio (*m*/*n*) can be fitted to the following equation, $E_f(\mathrm{He}_m\mathrm{V}_n) = 0.591(m/n)^2 - 0.566(m/n) + 0.335$. This fitted equation only works as the He/V ratio changes from ~0.4 to ~1.25. Consequently, the binding energy of one He atom in the bubble can be approximated as

$$E_b = 1.182\left(\frac{m}{n}\right)\frac{1}{n} - 0.591\frac{1}{n^2} - 0.566\frac{1}{n} - 5.225 \qquad (4)$$

The value of -5.225 is the formation energy of one He interstitial in Be in the units of eV. Eq. (4) shows that for a large-size bubble, the binding energy, E_b, of one He atom within the bubble consisting of *m* He atoms and *n* vacancies is always negative, suggesting the bubble will attract an additional He atom. It also shows that for a given size bubble, the binding energy of He atom in the bubble becomes less negative as the number of He atoms increases. One of the most important implications of our calculations is that the binding energy of one He atom in the bubble consisting of *m* He atoms and *n* vacancies will be primarily determined by the He/V ratio, as has been found for other materials [27].

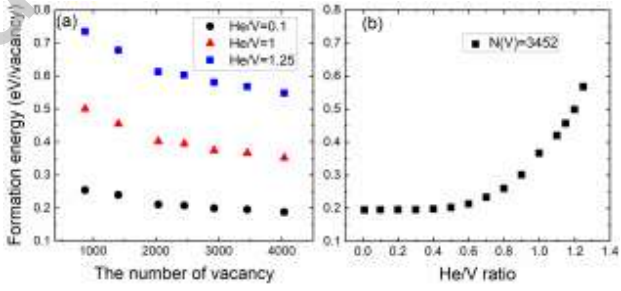

Fig. 4. Formation energy of He bubbles per vacancy (a) as a function of bubble size measured as the number of Be vacancies and (b) as a function of the He/V ratio.

3.4 Diffusion of He bubbles in Be

We next consider bubble migration energies of He bubbles. There have been multiple bubble migration mechanisms reported in the literature [37], and they include surface diffusion, volume diffusion, and vapor transport mechanisms. The vapor transport mechanism is dominant when the bubble size is on the order of micrometer [37], which is much larger than the bubble size that we are interested in this work. Therefore, here, we will mainly consider the surface and volume diffusion mechanisms. For the mechanism of surface diffusion, where the diffusion pathway of one Be atom is tangential to the bubble surface, the bubble diffusion coefficient D_B can be calculated using the following equation [14]

$$D_B = {}^{3}/_{2\pi}\ D_S({}^{\Omega^{\frac{1}{3}}}/_{r})^4 \quad (5)$$

Here, $\Omega = 8.11 \times 10^{-30}$ m^3 is the atomic volume of Be atom and r is the mean radius of the He bubble. It should be noted that since He bubbles in Be are ellipsoid-like, the bubble radius is not well defined. As an approximation, we assume the bubble shape to be spherical. $D_S = D_0^S \exp({}^{-E_m^S}/_{k_B T})$ is the surface diffusion coefficient of Be, where D_0^S and E_m^S are the pre-exponential factor and the migration energy for the surface diffusion, respectively, which can be obtained from MD simulations. The bubble equilibrated in our simulations has the following surfaces: {0001}, {10-10}, {10-11}, and {20-21}. Therefore, the average diffusion coefficient of He bubble via the surface diffusion mechanism would depend on the areal fraction of those surfaces in the bubble and the self-diffusion coefficient on each surface. In the following table (Table 3 in the response letter or Table 3 in the revised manuscript), we listed estimates of the areal fraction of each surface. This table shows that the fraction of the {0001} surface is dominant in the bubble, followed by the {10-11} surface. In addition, the calculated migration barrier of one vacancy on the {10-11} surface (0.23 eV) is comparable with that on the {0001} surface (0.22 eV). Considering the similar chemical bonding environment of Be on those different surfaces, it is reasonable to assume that the migration barriers of the vacancy on those surfaces are comparable. Therefore, the average diffusion coefficient of He bubble via the surface diffusion mechanism would be mainly determined by the areal fraction of those surfaces, which would be dominated by the diffusion on the {0001} surface.

Table 3. The areal fraction of each surface in the ellipsoid bubble after equilibrium

Surface	Areal fraction
{0001}	76.8%
{10-10}	5.1%
{10-11}	11.1%
{20-21}	7.0%

For the volume diffusion, where the diffusion flux of Be atom is normal to the surface, the bubble diffusion coefficient can be determined from the following equation [14]

$$D_B = {}^{3}/_{4\pi}\ D_V\left({}^{\Omega}/_{r^3}\right). \quad (6)$$

Here, $D_V = D_0^V \exp({}^{-E_m^V}/_{k_B T})$ is the volume diffusion coefficient of Be, and D_0^V and E_m^V are the pre-exponential factor and the migration energy for the Be volume diffusion, respectively. The surface and volume diffusivity at a given temperature can be calculated from the mean-square displacement (MSD) in the directions tangential to the surface by using the Einstein relation $D_{S/V} = \frac{1}{2d}\lim_{t\to\infty}\frac{d}{dt}(MSD(t))$, here d is the number of dimensions of motion. For the surface diffusion d=2, and for the volume diffusion d=3. Over time the MSD becomes linear due to the diffusion process and the surface/volume diffusivity is calculated by curve fitting the MSD data to the linear portion of the graph. By calculating the surface/volume diffusivity at different temperatures, the pre-exponential factor and the migration energy can be determined, as listed in Table 4.

Table 4. The diffusion coefficient pre-exponential factor and migration energy for the surface and volume diffusion of Be. Here the diffusion on the {0001} surface is considered.

Parameter	Pre-exponential factor (m^2/s)	Migration energy (eV)
Surface diffusion	5.90×10^{-12}	0.22
Volume diffusion	9.12×10^{-11}	0.46

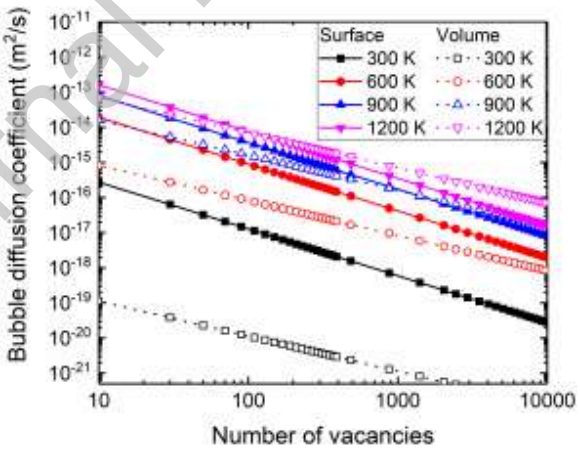

Fig. 5. Bubble diffusion coefficient determined by assuming surface and volume diffusion mechanisms at different temperatures as a function of the bubble size. The bubble size is quantified by the number of vacancies in the bubble.

We use Eqs. (5) and (6) to calculate the bubble diffusion coefficient as a function of the temperature and the bubble size for both the surface diffusion mechanism and the volume diffusion mechanism. As shown in Fig. 5, in the lower range of temperature, diffusion by the

surface mechanism is faster (i.e., it has a higher diffusion coefficient) than diffusion by the volume mechanism. This trend is reversed as the temperature is higher than ~900 K, especially for the large size bubbles. This finding is consistent with previous reports that the dominant diffusion mechanism could shift from surface diffusion to volume diffusion as temperature increases [37]. In Fig. 6, we further analyze the maximum size of bubbles that are mobile at different temperatures. Here, we consider the bubble to be mobile when it can diffuse ~100 nm (the diffusion distance is chosen to represent the average distance between bubbles for the bubble density of ~10^{21} m^3 [2,3]) within a certain time interval so that it can encounter other bubbles and react with them. The time interval of 1 hour is taken as an example, which is on the same order of timescale as the duration of ion irradiation experiments. Data in Fig. 6 shows that the maximum size for the mobile bubble increases as temperature increases, suggesting a possible coalescence of large bubbles in the high temperature regime, which can lead to significant bubble growth. For example, at ~700 K, one can see the bubble with ~3 nm can be mobile to coalesce with an additional one and form a larger bubble. As temperature increases, this coalescence reaction can occur between larger bubbles to cause the formation of the even larger one, which may explain the observation of increasing bubble size as irradiation temperature increases [2,3]. However, one should note that the formation of large bubbles depends not only on the bubble diffusivity but also on the bubble density and on the microstructure of the material. For example, if the bubble density is low enough, it is difficult to encounter another bubble in the sample, or if the bubble interacts with the interfaces, like grain boundaries, it would be trapped in grain boundary regions. Therefore, a full understanding of the bubble evolution in the material will require multiscale modeling. Our atomic-level modeling results here can provide the necessary parameters for such multiscale simulations.

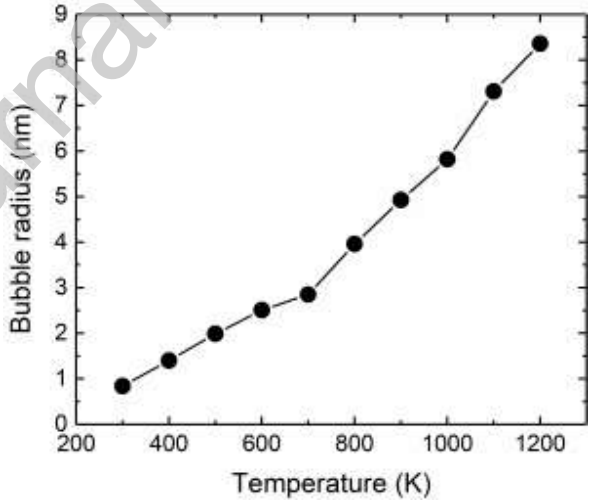

Fig. 6. The maximum size of a mobile bubble as a function of temperature. A bubble is considered mobile if it can diffuse ~100 nm within 1 hour.

4. Conclusion

Properties of He bubbles in Be were investigated using atomistic simulations. The shape and stability of He bubbles as a function of the He/V ratio are identified. Specifically, we find that regardless of the He/V ratio, the shape of He bubble in Be is ellipsoid-like, which is consistent with earlier experimental observations [2,3]. The punch-out reactions can occur as the ratio of He/V is larger than ~1.25, and these reactions can induce formation of dislocations around the bubble. The formation of He bubble in Be is also discussed. For a given He/V ratio, the bubble formation energy decreases as the number of vacancies in the bubble increases, indicating that the He bubble tends to attract vacancies to grow. Nevertheless, if the bubble size is constant, the formation energy of the bubble increases as the He/V ratio increases, suggesting that adding He atoms to the bubble can increase the bubble formation energy. However, the negative binding energy indicates that the bubble would still prefer to attract He atom to the bubble until the punch-out reaction occurs. We have also determined diffusion coefficients of He bubbles based on the surface and the volume diffusion mechanisms. The dominant diffusion mechanism is dependent on the temperature. In the low temperature regime, the surface diffusion mechanism is dominant, whereas the volume diffusion mechanism becomes more important and even dominant in the high temperature regime.

Acknowledgment

The authors grateful acknowledge financial support from the Department of Energy High Energy Physics Program grant DE-SC0020985 and from the Fermi National Accelerator Laboratory contract 663324.

References

[1] M. Klimenkov, P. Vladimirov, U. Jäntsch, V. Kuksenko, R. Rolli, A. Möslang, N. Zimber, New insights into microstructure of irradiated beryllium based on experiments and computer simulations, Sci. Rep. 10 (2020) 1–17. doi:10.1038/s41598-020-64654-5.

[2] M. Klimenkov, V. Chakin, A. Moeslang, R. Rolli, TEM study of beryllium pebbles after neutron irradiation up to 3000 appm helium production, J. Nucl. Mater. 443 (2013) 409–416. doi:10.1016/j.jnucmat.2013.07.050.

[3] N. Zimber, P. Vladimirov, M. Klimenkov, V. Kuksenko, Investigation of a high-dose irradiated beryllium microstructure, J. Nucl. Mater. 540 (2020) 152374. doi:10.1016/j.jnucmat.2020.152374.

[4] I.B. Kupriyanov, V.A. Gorokhov, R.R. Melder, Z.E. Ostrovsky, A.A. Gervash, Investigation of ITER candidate beryllium grades irradiated at high temperature, J. Nucl. Mater. 258–263 (1998) 808–813. doi:10.1016/S0022-3115(98)00383-3.

[5] N. Simos, M. Elbakhshwan, Z. Zhong, F. Camino, Proton irradiation effects on beryllium – A macroscopic assessment, J. Nucl. Mater. 479 (2016) 489–503. doi:10.1016/j.jnucmat.2016.06.048.

[6] N. Simos, H. Ludewig, H. Kirk, E. Dooryhee, S. Ghose, Z. Zhong, H. Zhong, S.

Makimura, K. Yoshimura, J.R.J. Bennett, G. Kotsinas, Z. Kotsina, K.T. McDonald, Multi-MW accelerator target material properties under proton irradiation at Brookhaven National Laboratory linear isotope producer, Phys. Rev. Accel. Beams. 21 (2018) 53001. doi:10.1103/PhysRevAccelBeams.21.053001.

[7] P. Hurh, K. Ammigan, B. Hartsell, R. Tschirhart, Targetry Challenges at Megawatt Proton Accelerator Facilities, in: Proc. 4th Int. Part. Accel. Conf., 2013: p. THPFI083.

[8] V. Kuksenko, K. Ammigan, B. Hartsell, C. Densham, P. Hurh, S. Roberts, Irradiation effects in beryllium exposed to high energy protons of the NuMI neutrino source, J. Nucl. Mater. 490 (2017) 260–271. doi:10.1016/j.jnucmat.2017.04.011.

[9] V.P. Chakin, Z. Ye Ostrovsky, Evolution of beryllium microstructure under high-dose neutron irradiation, J. Nucl. Mater. 307–311 (2002) 657–663. doi:10.1016/S0022-3115(02)01184-4.

[10] S.H. Li, J.T. Li, W.Z. Han, Radiation-induced helium bubbles in metals, Materials (Basel). 12 (2019). doi:10.3390/ma12071036.

[11] L. Sandoval, D. Perez, B.P. Uberuaga, A.F. Voter, Competing kinetics and he bubble morphology in W, Phys. Rev. Lett. 114 (2015) 1–5. doi:10.1103/PhysRevLett.114.105502.

[12] D. Perez, L. Sandoval, S. Blondel, B.D. Wirth, B.P. Uberuaga, A.F. Voter, The mobility of small vacancy/helium complexes in tungsten and its impact on retention in fusion-relevant conditions, Sci. Rep. 7 (2017) 1–9. doi:10.1038/s41598-017-02428-2.

[13] C. Dethloff, E. Gaganidze, V. V. Svetukhin, J. Aktaa, Modeling of helium bubble nucleation and growth in neutron irradiated boron doped RAFM steels, J. Nucl. Mater. 426 (2012) 287–297. doi:10.1016/j.jnucmat.2011.12.025.

[14] S.I. Golubov, R.E. Stoller, S.J. Zinkle, A.M. Ovcharenko, Kinetics of coarsening of helium bubbles during implantation and post-implantation annealing, J. Nucl. Mater. 361 (2007) 149–159. doi:10.1016/j.jnucmat.2006.12.032.

[15] J. Xi, B. Liu, H. Xu, Y. Zhang, W.J. Weber, Determination of gaseous fission product behavior near the cerium dioxide Σ3 (111)/[11¯0] tilt grain boundary via first-principles study, J. Nucl. Mater. 499 (2018) 377–382. doi:10.1016/j.jnucmat.2017.11.046.

[16] P. V. Vladimirov, A. Moeslang, Ab initio static and molecular dynamics studies of helium behavior in beryllium, J. Nucl. Mater. 442 (2013) 694–698. doi:10.1016/j.jnucmat.2013.04.041.

[17] M.G. Ganchenkova, P. V. Vladimirov, V.A. Borodin, Vacancies, interstitials and gas atoms in beryllium, J. Nucl. Mater. 386–388 (2009) 79–81. doi:10.1016/j.jnucmat.2008.12.063.

[18] J.M. Cayphas, M. Hou, L. Coheur, The behaviour of helium in neutron irradiated beryllium: A molecular dynamics study, J. Nucl. Mater. 246 (1997) 171–179. doi:10.1016/S0022-3115(97)00102-5.

[19] X. Huang, C. Lv, H. Chu, Anomalous shape effect of nanosized helium bubble on the elastic field in irradiated tungsten, Sci. Rep. 11 (2021) 1–7. doi:10.1038/s41598-020-80167-7.

[20] K.D. Hammond, D. Maroudas, B.D. Wirth, Theoretical Model of Helium Bubble Growth and Density in Plasma-Facing Metals, Sci. Rep. 10 (2020) 1–10. doi:10.1038/s41598-020-58581-8.

[21] F. Sefta, N. Juslin, B.D. Wirth, Helium bubble bursting in tungsten, J. Appl. Phys. 114 (2013). doi:10.1063/1.4860315.

[22] S. Plimpton, Fast parallel algorithms for short-range molecular dynamics, J. Comput. Phys.

117 (1995) 1–19.
[23] A.P. Thompson, L.P. Swiler, C.R. Trott, S.M. Foiles, G.J. Tucker, Spectral neighbor analysis method for automated generation of quantum-accurate interatomic potentials, J. Comput. Phys. 285 (2015) 316–330. doi:10.1016/j.jcp.2014.12.018.
[24] M.A. Wood, M.A. Cusentino, B.D. Wirth, A.P. Thompson, Data-driven material models for atomistic simulation, Phys. Rev. B. 99 (2019) 1–12. doi:10.1103/PhysRevB.99.184305.
[25] N. Juslin, B.D. Wirth, Interatomic potentials for simulation of He bubble formation in W, J. Nucl. Mater. 432 (2013) 61–66. doi:10.1016/j.jnucmat.2012.07.023.
[26] D.E. Beck, A new interatomic potential function for helium, Mol. Phys. 14 (1968) 311–315. doi:10.1080/00268976800100381.
[27] K. Morishita, R. Sugano, B.D. Wirth, T. Diaz de la Rubia, Thermal stability of helium-vacancy clusters in iron, Nucl. Instruments Methods Phys. Res. Sect. B Beam Interact. with Mater. Atoms. 202 (2003) 76–81. doi:10.1016/S0168-583X(02)01832-3.
[28] M.A. Cusentino, M.A. Wood, A.P. Thompson, Suppression of helium bubble nucleation in beryllium exposed tungsten surfaces, Nucl. Fusion. 60 (2020). doi:10.1088/1741-4326/abb148.
[29] J.F. Ziegler, J.P. Biersack, The Stopping and Range of Ions in Matter BT - Treatise on Heavy-Ion Science: Volume 6: Astrophysics, Chemistry, and Condensed Matter, in: D.A. Bromley (Ed.), Springer US, Boston, MA, 1985: pp. 93–129. doi:10.1007/978-1-4615-8103-1_3.
[30] J. Xi, C. He, H. Zang, D. Guo, T. Yang, T. Bo, P. Zhang, Evolution of atoms with special coordination number in β-SiC with temperature, J. Nucl. Mater. 435 (2013). doi:10.1016/j.jnucmat.2013.01.001.
[31] J. Xi, C. Liu, I. Szlufarska, Effects of point defects on oxidation of 3C–SiC, J. Nucl. Mater. 538 (2020) 152308. doi:10.1016/j.jnucmat.2020.152308.
[32] J. Rahm, P. Erhart, WulffPack: A Python package for Wulff constructions, J. Open Source Softw. 5 (2020) 1944. doi:10.21105/joss.01944.
[33] G. Kresse, D. Joubert, From ultrasoft pseudopotentials to the projector augmented-wave method, Phys. Rev. B - Condens. Matter Mater. Phys. 59 (1999) 1758–1775.
[34] I. Ipatova, G. Greaves, S. Pacheco-Gutiérrez, S.C. Middleburgh, M.J.D. Rushton, E. Jimenez-Melero, In-situ TEM investigation of nano-scale helium bubble evolution in tantalum-doped tungsten at 800°C, J. Nucl. Mater. 550 (2021). doi:10.1016/j.jnucmat.2021.152910.
[35] T.L. Einstein, 5 - Equilibrium Shape of Crystals, in: T.B.T.-H. of C.G. (Second E. Nishinaga (Ed.), Elsevier, Boston, 2015: pp. 215–264. doi:https://doi.org/10.1016/B978-0-444-56369-9.00005-8.
[36] J. Beuers, S. Jönsson, G. Petzow, TEM-in situ deformation of beryllium single crystals-a new explanation for the anomalous temperature dependence of the critical resolved shear stress for prismatic slip, Acta Metall. 35 (1987) 2277–2287. doi:10.1016/0001-6160(87)90075-7.
[37] F.A. Nichols, Kinetics of Diffusional Motion of Pores in Solids, 30 (1969) 143–165.

Declaration of interests

☒ The authors declare that they have no known competing financial interests or personal relationships that could have appeared to influence the work reported in this paper.

☐The authors declare the following financial interests/personal relationships which may be considered as potential competing interests:

Credit author statement

Jianqi Xi and Yeqi Shi: Writing-original draft preparation, Data curation, Conceptualization, Simulation, Analysis. **Vitaly Pronskikh**: Calculating and Conceptualization. **Frederique Pellemoine**: Suggesting, Reviewing, and Editing. **Dane Morgan**: Supervision, Reviewing, and Editing. **Izabela Szlufarska**: Supervision, Reviewing, and Editing.